

SMA observations towards the compact, short-lived bipolar water maser outflow in the LkH α 234 region

J. M. Girart,^{1,2★} J. M. Torrelles,^{3†} R. Estalella,⁴ S. Curiel,⁵ G. Anglada,⁶
J. F. Gómez,⁶ C. Carrasco-González,⁷ J. Cantó,⁵ L. F. Rodríguez,⁷
N. A. Patel² and M. A. Trinidad⁸

¹*Institut de Ciències de l'Espai (CSIC-IEEC), Can Magrans, S/N, E-08193 Cerdanyola del Vallès, Catalonia, Spain*

²*Harvard-Smithsonian Center for Astrophysics, 60 Garden Street, Cambridge, MA 02138, USA*

³*Institut de Ciències de l'Espai (CSIC-IEEC) and Institut de Ciències del Cosmos (UB-IEEC), Martí i Franquès 1, E-08028 Barcelona, Catalonia, Spain*

⁴*Departament de Física Quàntica i Astrofísica (formerly Astronomia i Meteorologia) and Institut de Ciències del Cosmos (IEEC-UB), Universitat de Barcelona, Martí i Franquès 1, E-08028 Barcelona, Catalonia, Spain*

⁵*Instituto de Astronomía (UNAM), Apartado 70-264, 04510 México DF, Mexico*

⁶*Instituto de Astrofísica de Andalucía (CSIC), Apartado 3004, E-18080 Granada, Spain*

⁷*Instituto de Radioastronomía y Astrofísica (UNAM), 58089 Morelia, Mexico*

⁸*Departamento de Astronomía, Universidad de Guanajuato, Apdo. Postal 144, 36000 Guanajuato, Mexico*

Accepted 2016 July 7. Received 2016 July 5; in original form 2016 April 18

ABSTRACT

We present Submillimeter Array (SMA) 1.35 mm subarcsecond angular resolution observations towards the LkH α 234 intermediate-mass star-forming region. The dust emission arises from a filamentary structure of ~ 5 arcsec (~ 4500 au) enclosing VLA 1-3 and MM 1, perpendicular to the different outflows detected in the region. The most evolved objects are located at the southeastern edge of the dust filamentary structure and the youngest ones at the northeastern edge. The circumstellar structures around VLA 1, VLA 3, and MM 1 have radii between ~ 200 and ~ 375 au and masses in the ~ 0.08 – $0.3 M_{\odot}$ range. The 1.35 mm emission of VLA 2 arises from an unresolved ($r \lesssim 135$ au) circumstellar disc with a mass of $\sim 0.02 M_{\odot}$. This source is powering a compact (~ 4000 au), low radial velocity (~ 7 km s $^{-1}$) SiO bipolar outflow, close to the plane of the sky. We conclude that this outflow is the ‘large-scale’ counterpart of the short-lived, episodic, bipolar outflow observed through H $_2$ O masers at much smaller scales (~ 180 au), and that has been created by the accumulation of the ejection of several episodic collimated events of material. The circumstellar gas around VLA 2 and VLA 3 is hot (~ 130 K) and exhibits velocity gradients that could trace rotation. There is a bridge of warm and dense molecular gas connecting VLA 2 and VLA 3. We discuss the possibility that this bridge could trace a stream of gas between VLA 3 and VLA 2, increasing the accretion rate on to VLA 2 to explain why this source has an important outflow activity.

Key words: masers – stars: formation – ISM: individual objects: LkH α 234-VLA 2 – ISM: jets and outflows – ISM: molecules.

1 INTRODUCTION

Accretion discs and mass-loss processes with the presence of magnetic fields govern the formation of low-mass stars (e.g. Machida, Inutsuka & Matsumoto 2008; Frank et al. 2014; Rao et al. 2014). These mass-loss processes are non-steady, presenting pulsed events that are probably related to episodic increases in the accretion rates (e.g. Reipurth & Bally 2001; Pech et al. 2010; Audard et al. 2014).

In the case of high-mass protostars, there is increasing evidence that the associated outflows are also non-steady. This is seen, in particular, with the detection through Very Long Baseline Interferometry (VLBI) H $_2$ O maser observations of short-lived (tens of years), episodic outflow events, which are interpreted as due to variability in the accretion processes as in the case of low-mass protostars (e.g. Torrelles et al. 2001; Sanna et al. 2012; Trinidad et al. 2013; Carrasco-González et al. 2015).

Very recently, we extended these VLBI water maser studies towards the cluster of intermediate-mass young stellar objects (YSOs) close to the optically visible Herbig Be star LkH α 234 in the NGC 7129 star-forming region (Torrelles et al. 2014). The YSOs in this

* E-mail: girart@ieec.cat

† The ICC (UB) is a CSIC-Associated Unit through the ICE.

cluster (including the star LkH α 234) are grouped within a radius of ~ 5 arcsec (~ 4500 au at a distance of 0.9 kpc; see Kato et al. 2011 and references therein). Five of these YSOs show radio continuum emission: LkH α 234, VLA 1, VLA 2, VLA 3A, and VLA 3B (Trinidad et al. 2004), all of them, excepting VLA 1, with mid-infrared counterparts (Kato et al. 2011). From the absence of near-infrared emission in the J , H , and K bands of VLA 2 and VLA 3A+3B (hereafter VLA 3), but being bright in the L' , M' , and mid-infrared bands, Kato et al. (2011) concluded that these two objects are highly embedded protostars, having also associated H $_2$ O maser emission (Tofani et al. 1995; Umemoto et al. 2002; Trinidad et al. 2004; Marvel 2005, see also fig. 1 in Torrelles et al. 2014 showing the spatial distribution of the YSOs in the cluster). Our multi-epoch VLBI H $_2$ O maser observations (Torrelles et al. 2014) revealed a very compact (~ 0.2 arcsec, ~ 180 au), short-lived (kinematic age of ~ 40 yr), episodic, and highly collimated water maser bipolar outflow emerging from VLA 2. These results predicted the presence of an accretion disc associated with VLA 2 as well as a relatively compact bipolar molecular outflow when observed through thermal molecular lines.

In this paper, we present Submillimeter Array (SMA) dust continuum, and thermal molecular line observations at ~ 1 mm wavelengths carried out towards VLA 2 to detect and characterize the expected disc-YSO-outflow system at scales of a few hundred au (Section 2). We show the observational results in Section 3, discussing them in Section 4. The main conclusions of this research are presented in Section 5.

2 SMA OBSERVATIONS

The SMA observations were carried out on 2014 August 14 and September 1 in the very extended and extended configurations, respectively. The receiver was tuned to cover the 214.3–218.3 and 226.3–230.3 GHz frequency ranges in the lower (LSB) and upper side band (USB), respectively. The phase centre of the telescope was $\alpha(J2000.0) = 21^{\text{h}}43^{\text{m}}06^{\text{s}}.50$ and $\delta(J2000.0) = 66^{\circ}06'55''.2$. We used the flexible SMA ASIC correlator, which provides 48 consecutive spectral windows of 104 MHz width. Most of these spectral windows were set to have a spectral resolution of 1.6 MHz (i.e. 2.13 km s^{-1} at 230 GHz). However, some spectral windows, which included several lines (e.g. $^{34}\text{SO } 6_5-5_4$, $\text{SO}_2 22_{2,20}-22_{1,21}$, $\text{CH}_3\text{OH } 5_{1,4}-4_{2,2}$, H $_2$ S) were set to have a spectral resolution of 0.4 MHz and 0.8 MHz (0.53 and 1.06 km s^{-1} , respectively). Unfortunately these are not the brightest lines, so they are not the best choices to trace the kinematics of the gas. The gain calibrators were QSOs 1927+739 and 2009+724. The bandpass calibrator was 3c454.3. The absolute flux scale was determined from observations of MWC349a and Neptune. The flux uncertainty was estimated to be ~ 20 per cent. The data were calibrated using the MIR package¹ and imaged using the MIRIAD software (Sault, Teuben & Wright 1995).

Self-calibration (phase only) was performed using the continuum data. The derived gain solutions were applied to the molecular line data. The continuum maps at 1.35 mm (222.3 GHz) were obtained combining the USB and LSB, the two array configurations, and using robust weighting of 0. The resulting synthesized beam was $0.62 \text{ arcsec} \times 0.48 \text{ arcsec}$ with a position angle $\text{PA} \simeq 68^\circ$. The rms noise level for the continuum image was $\simeq 0.6 \text{ mJy beam}^{-1}$. For the molecular line data, the dust continuum emission was subtracted in the visibility space before obtaining the channel maps. The spectral

line maps presented here were obtained by using a robust weighting of 1.0, which yielded a synthesized beam of $0.81 \text{ arcsec} \times 0.67 \text{ arcsec}$ ($\text{PA} = 73^\circ$) for the LSB and of $0.77 \text{ arcsec} \times 0.63 \text{ arcsec}$ ($\text{PA} = 73^\circ$) for the USB. The figures were created using the GREG package (from the GILDAS² software).

3 RESULTS

3.1 Continuum

Fig. 1(a) shows the 1.35 mm continuum map of the LkH α 234 region obtained with the SMA. The emission appears extended and elongated about 5 arcsec (4500 au) in the NW-SE direction, engulfing all known sources but LkH α 234. The overall morphology of the emission agrees with previous, lower angular resolution, 1.35 mm interferometric observations (beam ~ 1.3 arcsec) by Fuente et al. (2001). The observed elongation is also seen, but at much larger scales (up to ~ 0.3 pc), by single-dish observation of the 1.35 mm continuum and CO isotopologues (Fuente et al. 2001).

Our subarcsecond angular resolution 1.35 mm images show four distinct peaks of emission coinciding with sources VLA 1, VLA 2, VLA 3 (Trinidad et al. 2004), and MM 1 (Fuente et al. 2001). MM 1 is the only source not detected at other wavelengths. For all the mm continuum sources detected with the SMA and reported in this paper, there is a systematic position offset of ~ 0.2 arcsec with respect to the positions measured in the literature at other wavelengths (e.g. Fuente et al. 2001; Trinidad et al. 2004). This value is comparable to the absolute astrometric uncertainty in a typical SMA observation. In order to correct for the offset, we have used as a reference position the radio continuum position of VLA 2 (the most compact source both at cm and mm wavelengths), $\alpha(J2000) = 21^{\text{h}}43^{\text{m}}06^{\text{s}}.321$, $\delta(J2000) = 66^{\circ}06'55''.95$ given by Trinidad et al. (2004), assuming that the SMA mm continuum peak position of VLA 2 is the same as the VLA 2 position measured at cm wavelengths. This means that we had to apply a small astrometric correction of (-0.19 arcsec, 0.12 arcsec) to our SMA data, resulting also in an excellent alignment for all the other sources (see Fig. 1).

The total flux detected in the region by the SMA at 1.35 mm is $363 \pm 5 \text{ mJy}$. To compare this value with the one measured by Fuente et al. (2001) with the IRAM Plateau de Bure interferometer (PdBi) with an angular resolution of ~ 1.3 arcsec at 1.22 mm we used the dust continuum spectral index of 2.4 derived by these authors. In this way, we find that the SMA recovers about 90 per cent of the flux measured by the PdBi. This is ~ 65 per cent of the total flux measured with the IRAM 30m bolometer (Fuente et al. 2001).

Since there is extended 1.35 mm continuum emission around the four detected sources (VLA 1, VLA 2, VLA 3, and MM1), images have also been made by discarding the visibilities for baselines shorter than 100 $\text{k}\lambda$. This allowed us to resolve out the extended filamentary emission and to leave only the emission arising from the four sources. Fig. 1(b) shows the resulting map (which yielded a synthesized beam of $0.58 \text{ arcsec} \times 0.43 \text{ arcsec}$, $\text{PA} \simeq 72^\circ$), whereas Table 1 gives the positions, fluxes, and the deconvolved sizes by Gaussian fitting of the four sources. In VLA 3, the brightest source, the emission arises from a region with a radius of ~ 155 au, suggesting that the dust emission may arise from a circumbinary disc around VLA 3A and VLA 3B. MM 1 and VLA 1 appear to have

¹ <https://www.cfa.harvard.edu/~cqi/mircook.html>

² GILDAS data reduction package is available at <http://www.iram.fr/IRAMFR/GILDAS>.

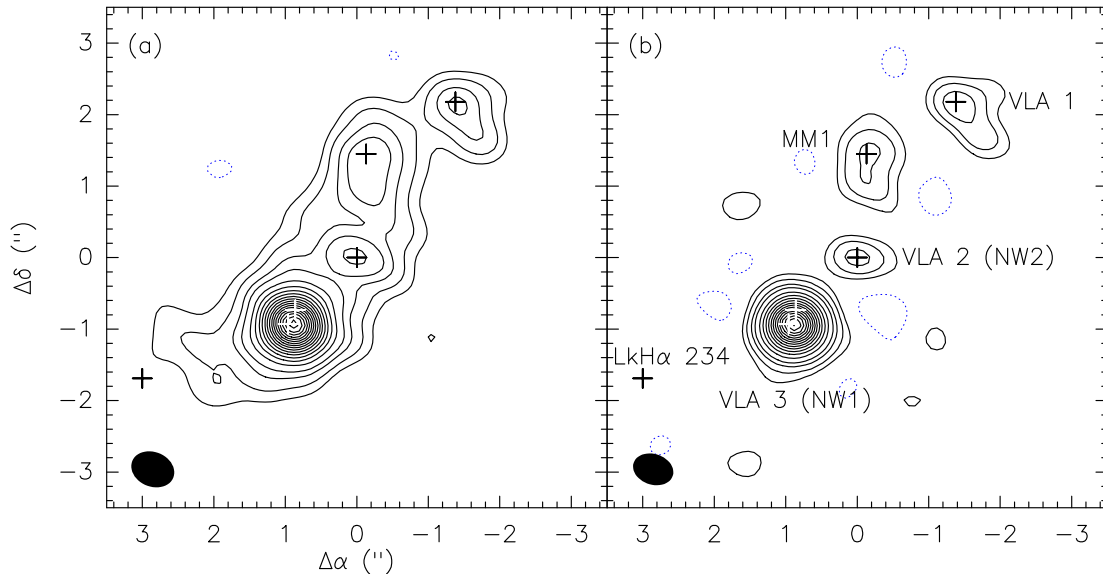


Figure 1. Panel (a): contour map of the 1.35 mm continuum emission towards LkH α 234. Panel (b): same as (a) but using only the visibilities for baselines longer than 100 k λ . Contours are $-4, 4, 8, 14,$ and from 20 to 170 in steps of 10, times $0.6 \text{ mJy beam}^{-1}$. The crosses show the position of the YSOs previously reported: LkH α 234, VLA 1, 2, 3A and 3B are taken from Trinidad et al. (2004, VLA 3A is the source closer to the dust peak) and MM 1 from Fuente et al. (2001). The black ellipses show the synthesized beams for each map.

Table 1. 1.35 mm continuum sources.

Source	α (J2000)	δ (J2000)	S_{ν} (mJy)	Deconvolved size ^a		PA ($^{\circ}$)	M^b (M_{\odot})	$n(\text{H}_2)$ (cm^{-3})	$N(\text{H}_2)$ (cm^{-2})
	$21^{\text{h}}43^{\text{m}}$ ($^{\circ}$)	$66^{\circ}6'$ ($''$)		Major axis, Minor axis (arcsec \times arcsec)					
VLA 3	6.461	55.00	139 ± 3	$0.44\pm 0.02\times 0.26\pm 0.02$	-22 ± 12	0.25	$1.8\ 10^9$	$5.4\ 10^{24}$	
VLA 2	6.321	55.95	12 ± 1	$\lesssim 0.3^c$		0.023	$\gtrsim 2\ 10^8$	$\gtrsim 6\ 10^{23}$	
MM 1	6.292	57.26	24 ± 2	$0.83\pm 0.15\times 0.24\pm 0.15$	-4 ± 10	$0.09\text{--}0.29$	$(3\text{--}9)\ 10^8$	$(1\text{--}4)\ 10^{24}$	
VLA 1	6.084	58.06	22 ± 2	$0.74\pm 0.15\times 0.23\pm 0.11$	35 ± 12	$0.08\text{--}0.26$	$(3\text{--}10)\ 10^8$	$(1\text{--}4)\ 10^{24}$	

Notes. ^aObtained by fitting a Gaussian with the *CASA imfit* task to each source in the image from Fig. 1(b). The major and minor axis are the full width at half-maximum values of the deconvolved size.

^bMass estimated from the dust emission assuming: optically thin emission, a gas to dust ratio of 100, a dust opacity per unit of dust mass of $1.1 \text{ cm}^2 \text{ g}^{-1}$ for VLA 2–3 and $0.9 \text{ cm}^2 \text{ g}^{-1}$ for MM 1 and VLA 1, which are the computed values by Ossenkopf & Henning (1994) at the observed wavelength and for dust particles with thin and thick ices, respectively. See Section 3.1 for the value of temperature used for each source.

^cThe source appears to be unresolved. The Gaussian fit yields an uncertainty for the major axis of 0.09 arcsec. We adopt an upper limit which is 3 times this uncertainty (i.e. at 3σ level).

not only similar fluxes but also similar sizes. Both sources are elongated, with major and minor semi-axes of ~ 370 and ~ 140 au, respectively, but with different orientations. VLA 2 appears to be unresolved, with a radius upper limit of ~ 135 au (Table 1). The total flux of the four compact sources is 197 ± 4 mJy. This leaves a flux that arises from the dust ridge of 166 ± 7 mJy.

The mass, volume, and column densities have been computed from the 1.35 mm dust emission of the four mm continuum sources (Table 1) assuming a constant temperature of 126 and 148 K for VLA 2 and VLA 3, respectively, which is the value derived from fitting the methanol and SO_2 lines. These two lines trace the hot and dense gas at similar scales as the dust (see Tables 1, 3, and Section 3.2). For MM 1 and VLA 1, we assume a temperature range of 30–80 K. The lack of methanol emission in these two sources suggests that it is depleted in the dust grain mantles (the methanol starts to sublimate at a temperature of ~ 80 K; Aikawa et al. 2008). Adopting a temperature of 22 K, derived from ammonia observations (Fuente et al. 2005), the mass of the dust ridge detected by the SMA is $\sim 7 M_{\odot}$.

3.2 Molecular lines

The SMA correlator provides 4 GHz of moderate spectral resolution data ($0.5\text{--}2.0 \text{ km s}^{-1}$). Table 2 shows the list of detected molecular transitions, including information of their frequencies and the energy of the lower rotational level. Regarding their morphology, there are two types of species. On one hand, there are several SO_2 and CH_3OH transitions, as well as a C_4H vibrational line, that have compact emission and are detected only towards VLA 2 and VLA 3. These transitions appear to have in most cases energy levels above 100 K. On the other hand, there are several molecular transitions that show extended emission. Fig. 2 shows the rich spectra over the whole observed bandwidth for VLA 2 and VLA 3. For comparison this figure also shows the VLA 1 spectrum.

3.2.1 Molecular ridges and extended structures around the YSOs

Fig. 3 shows the integrated emission for the five brightest lines that show extended emission. These images show a complex chemical

Table 2. Molecular lines detected.

Molecule	Molecular transition	ν^a (GHz)	E_l (K)	id. num. ^b
SO ₂	16 _{3,13} -16 _{2,14}	214.689 39	137.5	1
	17 _{6,12} -18 _{5,13}	214.728 29	218.7	2
	22 _{2,20} -22 _{1,21}	216.643 30	238.0	3
	14 _{3,11} -14 _{2,12}	226.300 03	108.1	4
	11 ₅₇ -12 _{4,8}	229.347 63	111.0	5
³⁴ SO ₂	4 _{2,2} -3 _{1,3}	229.857 63	7.56	6
CH ₃ OH	6 _{1,6} -7 _{2,5} $\nu_7=1$	215.302 20	363.5	7
	5 _{1,4} -4 _{2,2}	216.945 60	45.5	8
	6 _{1,5} -7 _{2,6} $\nu_7=1$	217.299 20	363.5	9
	20 _{1,19} -20 _{0,20}	217.886 39	497.9	10
	21 _{1,20} -21 _{0,21}	227.09460	546.2	11
	16 _{1,16} -15 _{2,13}	227.814 65	316.3	12
	15 _{4,11} -16 _{3,13}	229.589 07	363.4	13
	8-1, 8-7 _{0,7}	229.758 76	78.1	14
	3-2, 2-4-1, 4	230.027 06	28.8	15
	SO	5 ₅ -4 ₄	215.220 65	33.8
³⁴ SO	6 ₅ -5 ₄	215.839 92	4.0	17
H ₂ S	2 _{2,0} -2 _{1,1}	216.710 44	73.6	18
SiO	5-4	217.104 98	20.8	19
DCN	$J=3-2$	217.238 53	10.4	20
H ₂ CO	3 _{0,3} -2 _{0,2}	218.222 19	10.5	21
CN	2-1 3/2-1/2 ^c	226.659 56	5.4	
CN	2-1 5/2-3/2 ^d	226.874 78	5.4	
HC ₃ N	25-24	227.418 90	131.0	22
C ₄ H	47/2-45/2 ^e	228.539 42	316.9	23

Notes. ^aFrequency from the Cologne Database for Molecular Spectroscopy (Müller et al. 2001).

^bIdentification number shown in Fig 2.

^cThe complete transition name is $N=2-1 J=3/2-1/2 F=5/2-3/2$.

^dThe complete transition name is $N=2-1 J=5/2-3/2, F=7/2-5/2$. This line is blended with the $J=3/2-1/2 F=5/2-3/2$ and $J=5/2-3/2 F=3/2-1/2$ lines.

^eThe complete transition name $J=47/2-45/2, \Omega=1/2, l=f, \nu_7=1$.

Table 3. Molecular emission sizes of VLA 2 and VLA 3^a.

Source and line	FWHM (arcsec \times arcsec)	PA ($^\circ$)
CH ₃ OH 8-1, 8-7 _{0,7}		
VLA 2(NW2)	0.51 \pm 0.11 \times 0.37 \pm 0.11	73 \pm 23
VLA 3(NW1)	0.66 \pm 0.11 \times 0.43 \pm 0.13	-18 \pm 28
SO ₂ 16 _{3,13} -16 _{2,14}		
VLA 2(NW2)	0.53 \pm 0.22 \times 0.36 \pm 0.22	-52 \pm 70
VLA 3(NW1)	0.36 \pm 0.12 \times 0.15 \pm 0.20	-47 \pm 44

Note. ^aDeconvolved sizes obtained by fitting a Gaussian to each source using the *CASA imfit* task. We use the integrated emission images from Fig. 7.

behaviour, where each species traces slightly different regions of the LkH α 234 molecular gas environment. In order to simplify the description, we label in Fig. 3 the different molecular structures. Hereafter, we refer to the ‘dust ridge’ as the molecular structure that approximately traces the dust emission, as shown in Fig. 1(a). The ‘S ridge’ is the curved structure that extends to the south of VLA 2. The ‘LkH α 234 SE ridge’ is the structure seen only in SO to the south-east of LkH α 234. Finally, the ‘LkH α 234 NE ridge’ is the structure seen to the north-east of LkH α 234. The length of the different ridges is ~ 5 arcsec (~ 4500 au), except for the dust ridge that in SO has a length of ~ 10 arcsec (~ 9000 au). The width of the ridges is roughly ~ 2 arcsec (~ 1800 au). Below, we briefly describe the main properties of the spatial distribution of the different molecular transitions.

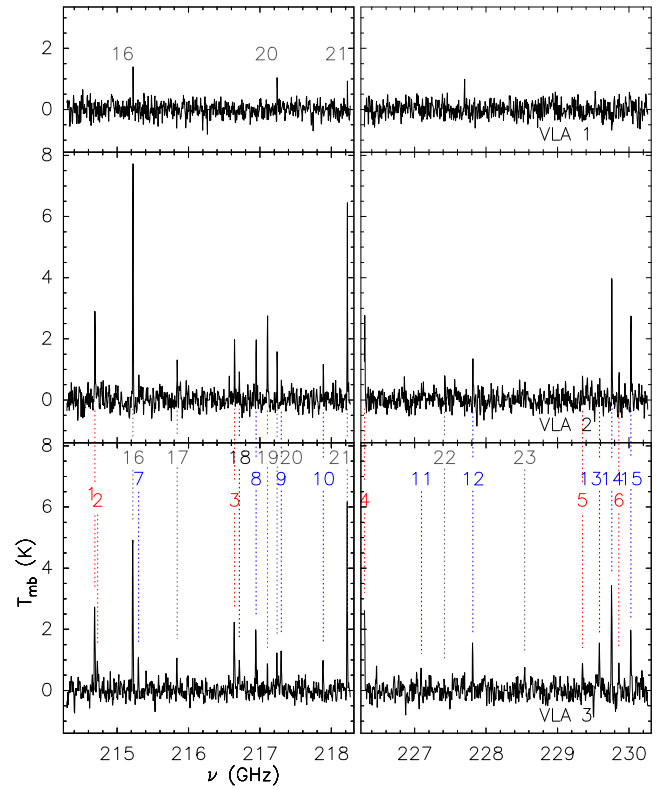


Figure 2. SMA spectra obtained at the position of the dust intensity peak of VLA 1, VLA 2, and VLA 3. Blue and red dotted lines show the CH₃OH and SO₂ lines, respectively. Grey dotted lines show other molecular transitions detected. The number is the identification label in Table 2. The conversion from flux density to main beam brightness temperature is ~ 47 K Jy⁻¹ at the observed frequencies and angular resolution.

(i) The SO 5₅-4₄ line traces all the aforementioned structures except the LkH α 234 NE ridge. There is copious SO emission around all the sources, with the peak emission arising towards VLA 2 and VLA 3.

(ii) The H₂CO line is the second most extended tracer, being detected in all structures except the LkH α 234 SE ridge. As in the case of the SO line, the strongest emission arises from VLA 2 and VLA 3.

(iii) The CN emission clearly traces the LkH α 234-NE ridge. There is also fluffy emission around, but not peaking at, VLA 1 and MM 1.

(iv) The DCN emission traces mostly the dust ridge although there is a void around VLA 3. There is also some emission along the LkH α 234 SE ridge.

(v) The HC₃N 25-24 line is only detected around VLA 2 and towards the LkH α 234-NE ridge.

(vi) The SiO 5-4 line emission (Fig. 4) appears to be detected around VLA 2 and VLA 3 and along the S ridge. However, there are significant differences with respect to the other tracers. There is blue and redshifted emission forming a compact (total length of ~ 4 arcsec or ~ 4000 au), low velocity (outflow velocities of ~ 7 km s⁻¹ with respect to the VLA 2 systemic velocity, ~ -11.5 km s⁻¹; see next subsection), bipolar outflow in the north-east-south-west direction (PA $\sim 20^\circ$), that is centred on VLA 2. The northern blueshifted lobe exhibits some weak redshifted emission. This, and the low radial velocity of the outflow suggest that the outflow axis is close to the plane of the sky (see also Section 4.1.2).

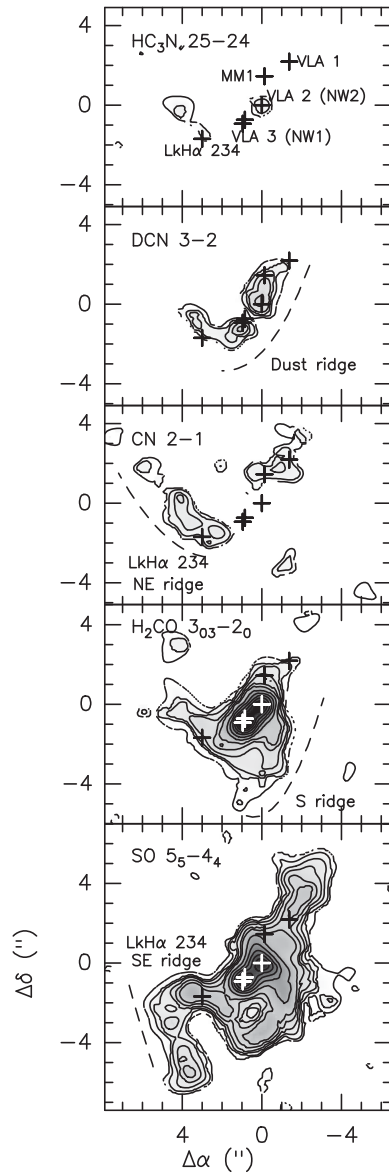


Figure 3. Integrated emission over the V_{LSR} velocity range between -15.2 and -3.8 km s^{-1} for several molecular transitions that show extended emission. Contours are 0.15, 0.3, 0.45, 0.6, 0.8, 1.0, 1.5, 2.0, 2.5, 3.0, 3.5, 4.0 Jy km s^{-1} . The crosses mark the positions of the different YSOs in the region.

At ~ 2 arcsec south-west of VLA 2 the redshifted emission bends to the east following the SE ridge.

The radial velocity maps of the molecular gas are shown in the (a) and (b) panels of Fig. 5 for the H_2CO and SO lines, respectively. There are complex velocity gradients, but the two more interesting ones are: (i) a mostly smooth gradient along the dust ridge, and (ii) a gradient along the S ridge (better seen in the H_2CO line). The second-order moment map of the $\text{SO } 5_5-4_4$ line shows that, except for VLA 2 and VLA 3, the typical velocity dispersion of the molecular gas is $\sim 1.0-1.5 \text{ km s}^{-1}$ (panel c of Fig. 5), which implies a line width of $\sim 2.4-3.4 \text{ km s}^{-1}$. Since the spectral resolution is $\sim 2.3 \text{ km s}^{-1}$, the line widths are barely resolved. The typical velocity dispersion corrected from the channel width is $\lesssim 1.2 \text{ km s}^{-1}$. The velocity dispersion increases towards VLA 2 and VLA 3 ($\gtrsim 2.0 \text{ km s}^{-1}$).

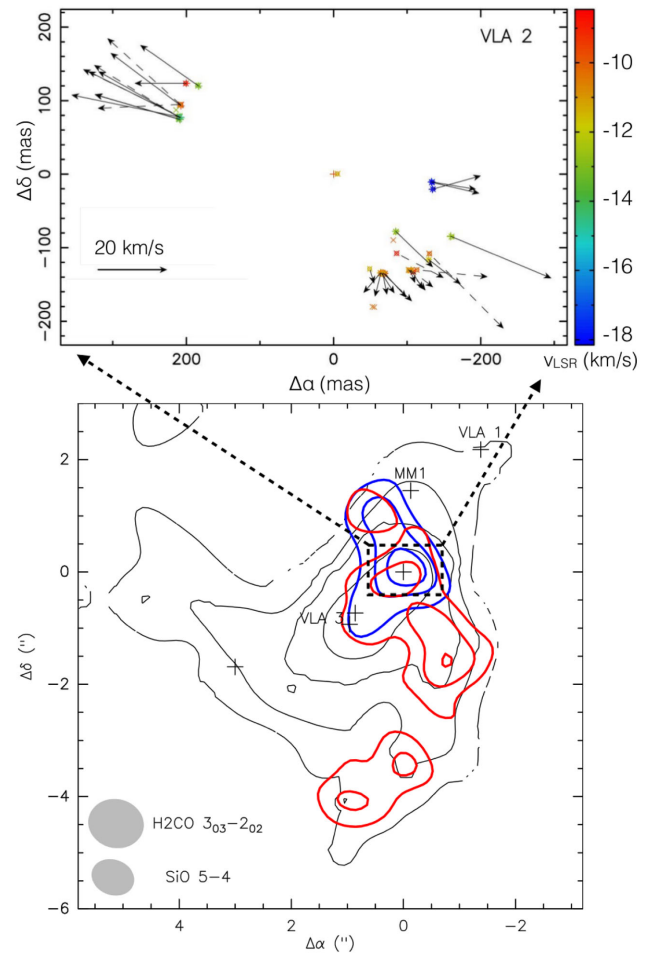


Figure 4. Bottom panel: overlap of the $\text{H}_2\text{CO } 3_{03}-2_{02}$ integrated emission (black contours) with the redshifted (V_{LSR} from -11.5 to -4.5 km s^{-1}) and blueshifted (V_{LSR} from -18.5 to -11.5 km s^{-1}) $\text{SiO } 5-4$ averaged emission (red and blue contours). The grey ellipses in the bottom part of the panel show the synthesized beam of these two lines. The crosses mark the different YSOs of the region as in Figs 1 and 3. H_2CO contours are 0.17, 0.56, 1.0, and 2.5 $\text{Jy beam}^{-1} \text{ km s}^{-1}$. SiO contours are 0.03, 0.06, 0.09, and 0.12 Jy beam^{-1} . Upper panel: Close-up of the proper motions of the H_2O masers associated with VLA 2 (from Torrelles et al. 2014).

3.2.2 The circumstellar environment around VLA 2 and VLA 3

The SO_2 and CH_3OH lines (Table 2) are only detected towards VLA 2 and VLA 3. Most of these lines can only be effectively excited if the gas is very dense and hot (because of their critical densities and energy levels; e.g. Table 2).

The SO_2 and CH_3OH lines were used to estimate the temperature of VLA 2 and VLA 3. We performed a rotational temperature diagram analysis³ using the transitions 1, 2, 3, and 5 of SO_2 , and the transitions 7–15 of CH_3OH (Table 2). The transition 4 of SO_2 was not used because of its location at the edge of the bandpass. The energies of the transition levels covered a wide range between 30 and 550 K. The fit of the integrated line intensity of the transitions

³ That is, we fit $\log(\int T_{\text{mb}} dv / S \mu^2) \propto E_u / T$, where $\int T_{\text{mb}} dv$ is the integrated intensity of a line transition, S the so-called line strength of the transition, μ the electric dipole moment for the molecule, E_u the energy level of the upper transition (in K) and T the gas temperature (e.g. Girart et al. 2002).

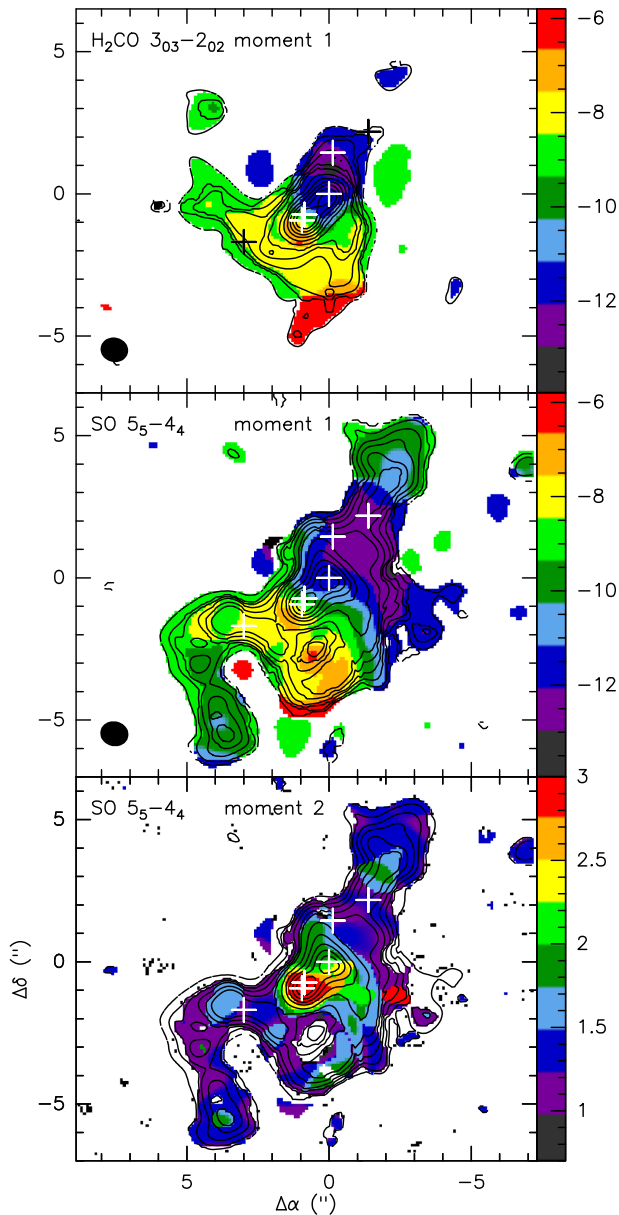


Figure 5. Panels (a) and (b): colour image of the first-order moment (velocity field) overlapped with the integrated emission of the H₂CO 3₀₃-2₀₂ and SO 5₅-4₄ lines, respectively. The colour wedge shows the velocity scale in km s⁻¹. Panel (c): second-order moment (velocity dispersion) overlapped with the integrated emission of the SO 5₅-4₄ line. The wedge indicates the velocity dispersion range in km s⁻¹. The crosses indicate the positions of the YSOs as in Figs 1 and 3.

over $S\mu^2$ versus the energy level gave us consistent values of the slope for both molecules, for VLA 2 and VLA 3. The value of the slope is inversely proportional to the rotational temperature, assumed to be the same for all the transitions of the same species. Finally, we obtained rotational temperature values of 126 ± 17 and 148 ± 21 K for VLA 2 and VLA 3, respectively (this is the error-weighted average of the SO₂ and CH₃OH temperatures, see Fig. 6)

Fig. 7 shows the integrated emission as well as the velocity map of the SO₂ and CH₃OH strongest lines. The molecular emission is quite compact, although around VLA 3 it is slightly elongated

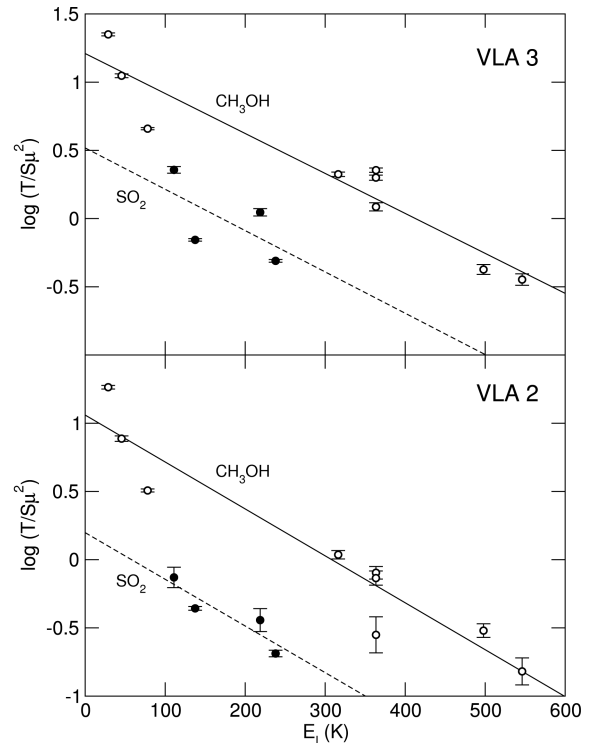


Figure 6. Population diagrams for the SO and the CH₃OH. Open and filled circles indicate the observed data for the CH₃OH and SO₂ transitions, respectively. The error bars include the measurement uncertainty and the calibration uncertainty (~ 15 per cent). The solid (CH₃OH) and dashed (SO₂) lines show the best fit obtained by assuming optically thin emission (i.e. using the standard population diagram analysis). For VLA 3, the best fit is for a temperature of 148 ± 15 and 144 ± 85 K for the CH₃OH and SO₂ data, respectively. For VLA 2, the best fit is 126 ± 13 K (CH₃OH) and 127 ± 28 K (SO₂).

along the north-west–south-east direction, with the molecular peaks of both species appearing closer to the continuum centimetre source VLA 3A than to VLA 3B. In order to measure their sizes, we fitted two Gaussians to the integrated emission shown in the aforementioned figure. This fit towards VLA 3 shows that the circumstellar molecular emission has a size and orientation similar to that of the dust emission (Tables 1 and 3). The CH₃OH and SO₂ emissions trace gas within ~ 300 and ~ 160 au (semimajor axes), respectively. Towards VLA 2 the size of the emission is similar for both lines (a semimajor axis of ~ 230 au).

The SO₂ and CH₃OH lines show a clear velocity gradient, with a total velocity change of ~ 12 km s⁻¹, along the major axis of VLA 3 (PA = -22° ; Table 1 and Fig. 7), which is similar to the direction of the velocity gradient seen at larger scale through other molecular lines (see Fig. 5).

Fig. 8 shows position–velocity plots along the axis that connects VLA 2 and VLA 3 (which is also the dust ridge major axis) for lines typical of warm/hot cores (CH₃OH, SO₂, H₂CO) overlapped with that from the SiO 5–4 line. There are several interesting behaviours in these position–velocity plots. (1) The centre velocity of the molecular emission of the two sources is different, ~ -11.5 km s⁻¹ and ~ -7 km s⁻¹ for VLA 2 and VLA 3, respectively. We note that the -11.5 km s⁻¹ value for VLA 2 is similar to the mean radial velocity of the H₂O masers associated with VLA 2, -11.6 km s⁻¹ (Torrelles et al. 2014). (2) There is a clear velocity gradient along

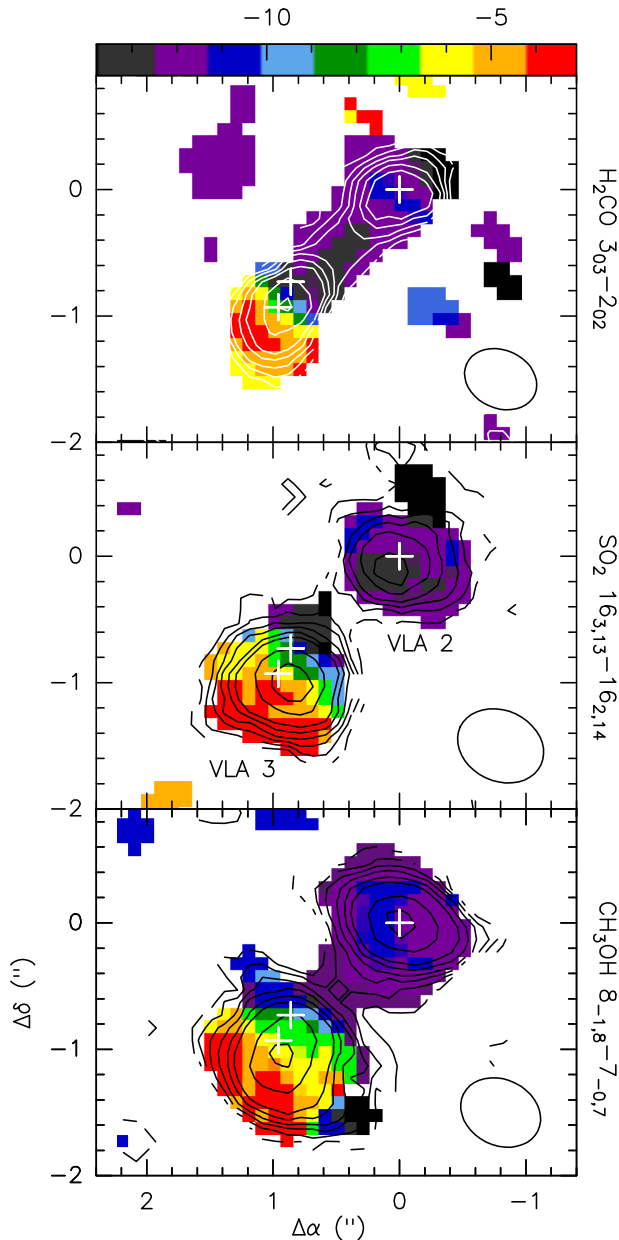


Figure 7. Colour image of the first-order moment (velocity field) of the $\text{H}_2\text{CO } 3_{0,3-2_{0,2}}$ (top panel), $\text{SO}_2 16_{3,13-16_{2,14}}$ (central panel) and $\text{CH}_3\text{OH } 8_{-1,8-7_{0,7}}$ (bottom panel) overlapped with the contour maps of their integrated emission towards VLA 2 and VLA 3. The wedge on the top indicates the velocity range (in km s^{-1}) of the three panels.

the major axis of VLA 3: north-west (blueshifted) to south-east (redshifted). In these plots, the emission at the 2σ contour level spans $\sim 20 \text{ km s}^{-1}$, although the most blueshifted emission is not detected in the CH_3OH line. Towards VLA 2, the molecular emission at the 2σ contour level spans over a smaller velocity interval, $\sim 12 \text{ km s}^{-1}$. However, the emission of the H_2CO and CH_3OH lines shows only a marginal velocity gradient (in the same direction as in VLA 3). (3) There is molecular gas between the two sources (as also seen in Fig. 7), with the most blueshifted gas in VLA 3 connected in velocity with a bridge of gas to VLA 2. (4) SiO is detected towards VLA 2 and towards the bridge of gas that connects to VLA 3.

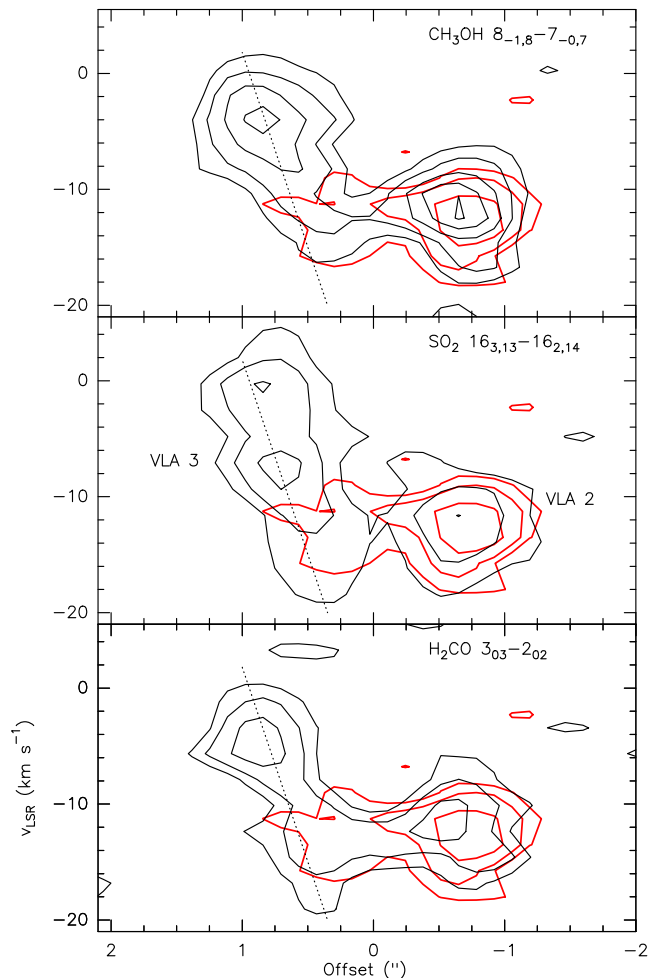


Figure 8. Position–velocity plots along the axis connecting VLA 2 and VLA 3 of the H_2CO (bottom panel), SO_2 (middle panel), and CH_3OH (top panel) lines (solid contours) overlapped with the $\text{SiO } 5-4$ line (red contours). The dotted line is shown to approximately mark the velocity gradient in VLA 3. The zero offset position corresponds to the intermediate position between VLA 3 and VLA 2 (see Section 4.1.3). The contour levels are 2, 4, 7, 10, and 13 times the rms noise of the maps, 23, 20, and 27 mJy beam^{-1} for the CH_3OH , SO_2 , and H_2CO lines, respectively. For the SiO line, the contours are 2, 3, and 5 times the rms noise of the map, 22 mJy beam^{-1} .

4 DISCUSSION

4.1 The intermediate-mass protostars VLA 2 and VLA 3

In this section, we discuss the properties of these two protostars and the possible interaction between their circumstellar material.

4.1.1 The masses of VLA 2 and VLA 3

The dense and warm circumstellar material at scales of 200 au (as traced by the 1.35 mm dust continuum emission) is about 10 times more massive in VLA 3 than in VLA 2 (~ 0.25 and $\sim 0.023 M_\odot$, respectively; Table 1). VLA 3 has a bolometric luminosity of $\sim 700 L_\odot$ (Kato et al. 2011). If all the luminosity would come from a single main-sequence star, then the stellar mass would be $\sim 6 M_\odot$. However, this is a binary (VLA 3A+VLA 3B) embedded YSO system, so this mass value is probably an upper limit for each of the two single components (in the case of twin components the mass of each component would be $\sim 5 M_\odot$), even more so considering that

part of the luminosity arises from the accretion. The stellar mass for VLA 2 is even more uncertain since the bolometric luminosity is unknown. Yet, its 11.8 μm flux is ~ 2.5 weaker than that of VLA 3 (Kato et al. 2011), which suggests that VLA 2 is also an intermediate-mass star. In fact, from the observed centimetre continuum emission of VLA 2, Torrelles et al. (2014) infer a bolometric luminosity of $\sim 50 L_{\odot}$ for this object which can be provided by a protostar of a few solar masses. An educated guess of the mass can be also done by comparing the velocity range of the emission for VLA 2 and VLA 3: at 2σ level the emission spreads out ~ 20 and 12 km s^{-1} for VLA 3 and VLA 2, respectively (see Section 3.2.2). If the kinematics is dominated by Keplerian motions (although with the present data we cannot discard the possibility that the motions around VLA 3 are just due to an overlapping of unbound motions of two independent sources, VLA 3A and VLA 3B), then the mass ratio between the two sources would be $M_2/M_3 = (R_3/R_2)(v_2/v_3)^2$, where the subindices 2 and 3 refer to VLA 2 and VLA 3. Assuming that the radius of emission, R , is approximately the same for the two sources (see section 3), then the VLA 2 mass is roughly 40 per cent smaller than the VLA 3, $\sim 2\text{--}4 M_{\odot}$.

4.1.2 The bipolar SiO outflow

The SiO 5-4 emission appears to originate from two different types of regions. First, there is a low radial velocity ($\sim 7 \text{ km s}^{-1}$) bipolar outflow in the north-east–south-west direction arising from VLA 2. Fig. 4 shows that the SiO is relatively compact (~ 4 arcsec, ~ 4000 au), especially in the blueshifted lobe and, more importantly, it is contained within the dense molecular gas structure traced by the $\text{H}_2\text{CO } 3_{0,3}\text{--}2_{0,2}$ line. As mentioned in Section 3.2.1, the relatively low radial velocities, with the northern blueshifted lobe also having weak redshifted emission, suggest that the outflow is close to the plane of the sky. There is also redshifted SiO emission ~ 4 arcsec south of VLA 3. If this emission is associated with the SiO bipolar outflow, then it would imply that the redshifted lobe has suffered a deflection of $\sim 50^\circ$.

We identify the bipolar molecular outflow seen in SiO as the ‘extended’ outflow counterpart of the very compact (~ 0.2 arcsec, ~ 180 au), short-lived (kinematic age ~ 40 yr), episodic, bipolar outflow observed through H_2O maser proper motions also expanding close to the plane of the sky in the north-east–south-west direction with velocities of $\sim 20 \text{ km s}^{-1}$ (Torrelles et al. 2014, see Fig. 4). In fact, from the proper motions and radial velocities of the H_2O masers reported by Torrelles et al. (2014) we estimate that the outflow axis has an inclination angle of $\sim 15^\circ$ with respect to the plane of the sky. From the observed spatial extension and radial velocity of the SiO bipolar outflow, we estimate a kinematic age of ~ 350 yr for this outflow (after correcting for the inclination angle of $\sim 15^\circ$). We therefore propose that this more extended and ‘older’ outflow seen in SiO has been created by the accumulation of the ejection of several episodic collimated events of material as the one observed through the H_2O masers. We note, however, that the position angle of the SiO bipolar outflow is $\sim 206^\circ$, while the position angle of the very compact H_2O maser outflow is $\sim 247^\circ$ (Torrelles et al. 2014). It is possible that this difference in position angles of $\sim 40^\circ$ between the extended SiO outflow and the compact H_2O maser outflow is due to several short-lived episodic ejection events, which would have slightly different position angles at their origin.

4.1.3 A stream of gas between VLA 3 and VLA 2?

The other type of emission traced by SiO arises at the systemic velocity of the core (see Fig. 8). The SiO emission is a signpost of

strong shocks, since it can be generated after sputtering in shocks of the Si locked in the dust grains (Schilke et al. 1997). However, in other star-forming regions SiO is detected at velocities close to the systemic velocity of the cloud, with relatively narrow line widths and with no obvious association with the protostellar outflow activity (Jiménez-Serra et al. 2010; Nguyen-Lu’o’ng et al. 2013). It has been proposed that, in these cases, the SiO can be produced in low-velocity shocks ($\lesssim 10 \text{ km s}^{-1}$) if about 10 per cent of the Si is already in the gas phase or in the icy mantles (Nguyen-Lu’o’ng et al. 2013). Although this can explain the SiO emission at velocities close to the systemic velocity of the core, it is unclear what would be the origin of the initial Si abundance outside of the dust grains. SiO emission at velocities close to the systemic velocity of the cloud is detected both in VLA 2 and in the bridge of molecular emission connecting VLA 2 and VLA 3 (hereafter ‘VLA 3–2 bridge’; see Fig. 8). Thus, we think that this SiO emission is probably due to the interaction (resulting in low velocity shocks), either between the VLA 2 and VLA 3 circumstellar gas, or between the VLA 2 circumstellar gas and the dust ridge gas that surrounds the two circumstellar structures. This latter case is less probable, since the VLA 3–2 bridge shows emission from hot core-like molecular lines that are also present in VLA 2 and VLA 3, but not in the dust ridge. Therefore, we favour a kinematical scenario with a stream of gas between VLA 3 and VLA 2, producing shocks and releasing SiO. However, with the present data we cannot discern the direction of the stream of gas (either from VLA 3 to VLA 2 or from VLA 2 to VLA 3), particularly considering that VLA 3 is a binary source where we are not able to resolve the kinematics and spatial distribution of the gas contents of each component (3A and 3B). Nevertheless, if the stream of gas is from VLA 3 to VLA 2, this scenario would increase the accretion rate on to VLA 2, and could explain why this protostar has a high outflow activity.

4.2 Star formation on the dust ridge

Here, we discuss the apparently organized star formation process taking place in the dust ridge.

4.2.1 Outflows and the dust ridge orientation

The outflow activity detected in this region is diverse, but all the signposts indicate that there is a preferential direction of the various outflow axes (Trinidad et al. 2004). Besides the aforementioned H_2O maser and SiO outflows associated with VLA 2, VLA 3A, and VLA 3B are radio jets with position angles of $\sim 55^\circ$ and $\sim 57^\circ$, respectively (Trinidad et al. 2004). VLA 1 is also a radio jet with a position angle of $\sim 45^\circ$ (Trinidad et al. 2004). There is a large scale (~ 1 pc) NE-SW CO bipolar outflow, with the NE red lobe being more extended and brighter than the SW blue lobe (Edwards & Snell 1983; Fuente et al. 2001). Interestingly, and in spite of having a similar orientation as the SiO bipolar outflow (this paper), the CO outflow has an inverted velocity pattern, suggesting a different powering source. There are two additional jets south-west of the dust ridge. One detected in [S II] extending ~ 0.2 pc with PA $\simeq 252^\circ$ (Ray et al. 1990). The other one, in near-IR H_2 emission, extending ~ 0.05 pc with PA $\simeq 226^\circ$ (Cabrit et al. 1997). Fuente et al. (2001) suggest that the [S II] jet and the CO NE red lobe are powered by VLA 3, whereas the CO SW blue lobe and the molecular hydrogen jet are powered by MM 1. Recently, Oh et al. (2016) have detected a very high velocity blueshifted [Fe II] knot, a few arcseconds south of VLA 3, which appears to be associated with the VLA 3B radio jet. Finally, McGroarty, Ray & Bally (2004) detect

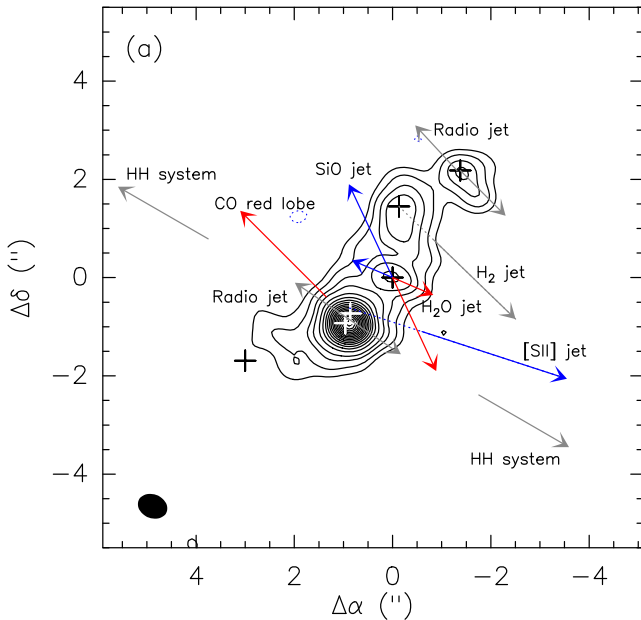


Figure 9. Contour map of the 1.35 mm continuum emission towards LkH α 234 (same as in Fig. 1), superposed with the direction of the different outflow signpost detected at different wavelengths (see Section 4.2.1). Blue and red arrows indicate blue and redshifted gas, whereas grey arrows show outflow direction without velocity information. The crosses mark the different YSOs in the region as in Fig. 1.

a chain of HH objects, HH 815-822, centred around the LkH α 234 region, with an outflow axis at PA=60°/240° and extending \sim 6 pc. However, the driving source of this HH system is unclear. Fig. 9 shows the dust emission traced by our SMA observations with the directions of the outflows identified in the region. It is clear that the overall trend of the activity of the outflows occurs in a direction that is approximately perpendicular to the dust ridge. We think that a magnetic field perpendicular to the dust ridge could produce the general alignment of the different outflows in the region. Although in general there is not a clear correlation between the magnetic field and the outflow direction at core scales, \sim 10³ au (Girart, Rao, & Marrone 2006; Hull et al. 2013; Zhang et al. 2014), there are some cases where they are aligned (Hull et al. 2014; Qiu et al. 2014; Zhang et al. 2014). This can be tested with dust polarization measurements along the dust ridge.

4.2.2 Organized star formation?

The most evolved source, LkH α 234, is located at the southeastern edge of the dust ridge, whereas the two apparently youngest sources, MM 1 and VLA 1, are located at the opposite side of the dust ridge. Our estimate of these sources being the youngest is based on two main facts. First, they are not detected at mid-IR or shorter wavelengths. Secondly, the circumstellar gas is as dense and massive as in VLA 2 and VLA 3, but it is significantly colder (there is no indication of hot core tracers as in VLA 2 and VLA 3). Therefore, these properties suggest an overall evolutionary sequence along the dust ridge, where star formation started in the southeastern part of the dust ridge and has proceeded with time towards the north-west. We speculate that a compression wave has continued towards the north-west extreme, once the star formation started in LkH α 234. This, together with the fact that the outflow activity occurs in a direction perpendicular to the dust ridge suggests that the present

star formation activity in the region around LkH α 234 is taking place in an organized fashion.

5 CONCLUSIONS

We report SMA 1.35 mm continuum and spectral line observations (angular resolution \sim 0.5–0.8 arcsec) towards the intermediate-mass star-forming region around the optically visible star LkH α 234.

We have detected a dust ridge of \sim 5 arcsec (\sim 4500 au) size containing the cluster of YSOs VLA 1, VLA 2, VLA 3A, VLA 3B, and MM1. The mass of the dust ridge is \sim 7 M_{\odot} , while the circumstellar masses around these YSOs are in the range of \sim 0.02–0.3 M_{\odot} . We find an evolutionary star formation sequence along the dust ridge, with the most evolved objects located at the southeastern edge of the ridge and the youngest ones located at the northeastern edge. The outflow activity of the different YSOs in the region occurs approximately perpendicular to the dust ridge. This overall trend of orientation of the outflows could be explained by the presence of a ‘large-scale’ magnetic field perpendicular to the dust ridge.

Our SMA observations reveal towards VLA 2, a compact (\sim 4 arcsec, \sim 4000 au), SiO bipolar outflow, moving close to the plane of the sky in the north-east–south-west direction. The kinematic age of the SiO outflow is \sim 350 yr. We conclude that this outflow is the ‘large-scale’ counterpart of the much more compact (\sim 0.2 arcsec, \sim 180 au), short-lived (\sim 40 yr), episodic, bipolar H₂O maser outflow previously reported with VLBI observations towards VLA 2. We propose that the bipolar outflow seen in SiO has been created by the accumulation of material through repetitive ejections of collimated gas as the one observed through the H₂O masers.

There is a bridge of molecular gas connecting VLA 3 and VLA 2 having SiO emission at ambient velocities. We discuss the possibility that this SiO ambient emission in the VLA 3–2 molecular bridge is due to an interaction of the gas transfer between VLA 3 and VLA 2. If the gas transfer occurs from VLA 3 to VLA 2 it could increase the accretion rate on to VLA 2, explaining the observed high outflow activity in this source.

ACKNOWLEDGEMENTS

GA, RE, JMG, JFG, and JMT acknowledge support from MINECO (Spain) AYA2014-57369-C3 grant (co-funded with FEDER funds). JMG also acknowledges support from the MECD PRX15/00435 grant (Spain) and from the SI CGPS award, ‘Magnetic Fields and Massive Star Formation’. RE also acknowledges MDM-2014-0369 of ICCUB (Unidad de Excelencia ‘María de Maeztu’). SC acknowledges the support of DGAPA, UNAM, and CONACyT (Mexico).

REFERENCES

- Aikawa Y., Wakelam V., Garrod R. T., Herbst E., 2008, *ApJ*, 674, 984
- Audard M. et al., 2014, in Beuther H., Klessen R. S., Dullemond C. P., Henning T., eds, *Protostars and Planets VI*. Univ. Arizona Press, Tucson, AZ, p. 387
- Cabrit S., Lagage P.-O., McCaughrean M., Olofsson G., 1997, *A&A*, 321, 523
- Carrasco-González C. et al., 2015, *Science*, 348, 114
- Edwards S., Snell R. L., 1983, *ApJ*, 270, 605
- Frank A. et al., 2014, in Beuther H., Klessen R. S., Dullemond C. P., Henning T., eds, *Protostars and Planets VI*. Univ. Arizona Press, Tucson, AZ, p. 451
- Fuente A., Neri R., Martín-Pintado J., Bachiller R., Rodríguez-Franco A., Palla F., 2001, *A&A*, 366, 873

- Fuente A., Rizzo J. R., Caselli P., Bachiller R., Henkel C., 2005, *A&A*, 433, 535
- Girart J. M., Viti S., Williams D. A., Estalella R., Ho P. T. P., 2002, *A&A*, 388, 1004
- Girart J. M., Rao R., Marrone D. P., 2006, *Science*, 313, 812
- Hull C. L. H. et al., 2013, *ApJ*, 768, 159
- Hull C. L. H. et al., 2014, *ApJS*, 213, 13
- Jiménez-Serra I., Caselli P., Tan J. C., Hernandez A. K., Fontani F., Butler M. J., van Loo S., 2010, *MNRAS*, 406, 187
- Kato E., Fukagawa M., Perrin M. D., Shibai H., Itoh Y., Ootsubo T., 2011, *PASJ*, 63, 849
- McGroarty F., Ray T. P., Bally J., 2004, *A&A*, 415, 189
- Machida M. N., Inutsuka S.-i., Matsumoto T., 2008, *ApJ*, 676, 1088
- Marvel K. B., 2005, *AJ*, 130, 2732
- Müller H. S. P., Thorwirth S., Roth D. A., Winnewisser G., 2001, *A&A*, 370, L49
- Nguyen-Lu'o'ng Q. et al., 2013, *ApJ*, 775, 88
- Oh H. et al., 2016, *ApJ*, 817, 148
- Ossenkopf V., Henning T., 1994, *A&A*, 291, 943
- Pech G., Loinard L., Chandler C. J., Rodríguez L. F., D'Alessio P., Brogan C. L., Wilner D. J., Ho P. T. P., 2010, *ApJ*, 712, 1403
- Qiu K., Zhang Q., Menten K. M., Liu H. B., Tang Y.-W., Girart J. M., 2014, *ApJ*, 794, L18
- Rao R., Girart J. M., Lai S.-P., Marrone D. P., 2014, *ApJ*, 780, L6
- Ray T. P., Poetzel R., Solf J., Mundt R., 1990, *ApJ*, 357, L45
- Reipurth B., Bally J., 2001, *ARA&A*, 39, 403
- Sanna A., Reid M. J., Carrasco-González C., Menten K. M., Brunthaler A., Moscadelli L., Rygl K. L. J., 2012, *ApJ*, 745, 191
- Sault R. J., Teuben P. J., Wright M. C. H. 1995, in Shaw R. A., Payne H. E., Hayes J. J. E., eds, *ASP Conf. Ser. Vol. 77, Astronomical Data Analysis Software and Systems IV*. Astron. Soc. Pac., San Francisco, p. 433
- Schilke P., Walmsley C. M., Pineau des Forets G., Flower D. R., 1997, *A&A*, 321, 293
- Tofani G., Felli M., Taylor G. B., Hunter T. R., 1995, *A&AS*, 112, 299
- Torrelles J. M. et al., 2001, *Nature*, 411, 277
- Torrelles J. M. et al., 2014, *MNRAS*, 442, 148
- Trinidad M. A., Curiel S., Torrelles J. M., Rodríguez L. F., Cantó J., Gómez J. F., Patel N., Ho P. T. P., 2004, *ApJ*, 613, 416
- Trinidad M. A. et al., 2013, *MNRAS*, 430, 1309
- Umemoto T., Imai H., Furuya R. S., Kitamura Y., Kawabe R., 2002, in Migenes V., Reid M. J., eds, *Proc. IAU Symp. 206, Cosmic Masers: From Proto-Stars to Black Holes*. Astron. Soc. Pac., San Francisco, p. 76
- Zhang Q. et al., 2014, *ApJ*, 792, 116

This paper has been typeset from a $\text{\TeX}/\text{\LaTeX}$ file prepared by the author.